Ceramics International 47 (2021) 14021–14032

Contents lists available at ScienceDirect

Ceramics International

journal homepage: www.elsevier.com/locate/ceramint

Controllable synthesis of sodium titanates using facile ball milling method

Mohamed Youssry *, Afnan Mussa

Department of Chemistry and Earth Sciences, College of Arts and Sciences, Qatar University, Doha, 2713, Qatar

ARTICLE INFO

Keywords:
Sodium titanates
Ball milling method
Mechanochemical activation
Milling energy
Tunnel-layered nanostructures

ABSTRACT

In this study, we demonstrated a controllable synthesis of sodium titanates ($Na_2Ti_6O_{13}$ and $Na_2Ti_3O_7$) using simple mechanochemical (dry ball milling) method. Although the titanates were obtained after calcination, however, the milling speed and duration control the phase type, crystallinity, purity and morphology of the as-synthesized materials. At low milling speed (200 rpm), cuboid-like $Na_2Ti_6O_{13}$ nanostructures were the dominant phase, where the purity and crystallinity enhanced for prolonged milling duration (20 h). The nanorod-like $Na_2Ti_3O_7$ phase is the dominant phase at higher milling speeds (≥300 rpm) with minor traces of $Na_2Ti_6O_{13}$ phase that disappeared at prolonged milling. In contrast to wet chemical methods, no byproducts such as titanic acids or unreacted materials were detected in the materials synthesized by the mechanochemical method.

1. Introduction

The past two decades have witnessed a massive growth of research interest in sodium titanate nanoceramics and their promising applications in energy storage systems [1,2], photocatalysis [3,4], sensing [5,6], and bioactive [7] properties. With the general formula; $Na_2Ti_nO_{2n+1}$ (n = 3–8), sodium titanates have a variety of crystalline phases with peculiar physicochemical properties. Particularly, sodium trititanate ($Na_2Ti_3O_7$) and sodium hexatitanate ($Na_2Ti_6O_{13}$) have been extensively studied as promising anode materials in sodium-ion batteries [1,2,8] due to their excellent stability, ionic conductivity and storage capability. Despite lower theoretical capacity [9], $Na_2Ti_6O_{13}$-based electrodes showed higher ionic conductivity, longer cycling stability and lower operational voltage than $Na_2Ti_3O_7$-based ones. $Na_2Ti_3O_7$ has a two-dimensional layered structure with three-stacked TiO_6 octahedra ribbons, whereas, $Na_2Ti_6O_{13}$ shows a three-dimensional tunnel structure with six TiO_6 octahedra that share edges [8]. Such different crystalline structure may explain the higher ionic conductivity and faster diffusivity of active Na^+ ions exhibited by $Na_2Ti_6O_{13}$ structures [10]. Beside the crystalline structure [11], the electrochemical performance of sodium titanates is unambiguously closely related to the morphology [12–15], particle size [16] and purity [9,10,17,18] of anode materials, and hence their packing and homogeneity when formulating the electrode. The synthesis method unequivocally influences the characteristics of sodium titanates.

Sodium titanates have been synthesized using various approaches, including the hydrothermal [9,12,13,19–21], solid-state reaction [1,11,15,22], sol-gel [5,7,23], and soft template [8] methods. Table S1 summarizes a comparison between the synthesis conditions and the characteristics of produced sodium titanates using the most common methods; hydrothermal and solid-state methods. The phase type ($Na_2Ti_3O_7$ or $Na_2Ti_6O_{13}$), purity, morphology, and particle size of the synthesized titanates are very sensitive to various key factors including: (i) the nature and concentration of starting materials, (ii) reaction duration and temperature, (iii) protocol of post-treatment, and (iv) calcination temperature and duration. As can been seen from Table S1, there is no simple correlation between the synthesis method (and conditions) and the characteristic of produced titanates. Roughly, the hydrothermal method mainly produces $Na_2Ti_3O_7$ [12,19,21,24,25] and rarely $Na_2Ti_6O_{13}$ [9,13,26] with nanotube/nanofiber morphologies. In addition, highly concentrated NaOH (sodium source), prolonged hydrothermal reaction at higher temperatures favorably produce $Na_2Ti_3O_7$ rather than $Na_2Ti_6O_{13}$ which is formed at diluted NaOH solution [9,26]. As a wet-chemistry, the hydrothermal method involves multi-step preparation including dispersing of starting materials and utilization of solvents, and more seriously washing by either water or acids. This results in protons (H^+) exchange Na^+ ions and eventually undesired protonated titanates are formed as byproducts [12,20,27–29].

The solid-state reaction (also called mechanochemical or ball milling) method is another common method that has been less used to prepare sodium titanates [1,11,15,22]. It regularly involves the mechanical mixing of starting materials followed by calcination at high temperature without post-treatment steps such as washing or purification. Therefore, titanic acids and other byproducts are not formed.

* Corresponding author. Department of Chemistry and Earth Sciences Qatar University, 2713, Doha, Qatar.
E-mail address: myoussry@qu.edu.qa (M. Youssry).

https://doi.org/10.1016/j.ceramint.2021.01.271
Received 21 August 2020; Received in revised form 27 December 2020; Accepted 28 January 2021
Available online 30 January 2021

Beside the calcination temperature and duration, the milling parameters (e.g. speed and duration) might have impact on the crystalline phase, purity, morphology and particle size of synthesized titanates. These parameters are rarely stated in the studies utilized the mechanochemical method to synthesize sodium titanates [11,22,30]. Accordingly, we believe that the inconsistency of phase type, purity, morphology and particle size of synthesized titanates is a consequence of uncontrolled milling parameters. For instance, Zhu et al. synthesized a pure $Na_2Ti_3O_7$ [31], whilst Dynarowska et al. obtained polyphasic titanates ($Na_2Ti_3O_7$ with traces of $Na_2Ti_6O_{13}$) [32] using the same solid-state method and precursor materials (TiO_2 anatase and anhydrous Na_2CO_3).

The mechanochemical method has been extensively used to directly synthesis various kinds of ceramic oxides [33–38] or simply activate the reactants [39,40] before calcination step. It is a robust simple method that enables controllable synthesis of the sodium titanates when the milling parameters are sensitively tuned. In this study, we attempt to systematically investigate the influence of milling parameters (i.e., milling speed and duration) on the phase type, crystallinity, purity and morphology of the synthesized sodium titanates.

2. Experimental

2.1. Materials and mechanochemical synthesis

Titanium (IV) oxide anatase (TiO_2, ≥99%), and anhydrous sodium carbonate (Na_2CO_3, ≥99%), were purchased, respectively, from Sigma-Aldrich and Fluka, USA. The materials have been kept at 70 °C in vacuum oven to avoid the hydration, and used without further purification.

The sodium titanates were synthesized using plenary ball mill (Changsha Tianchuang Powder Technology Co., Ltd). In 50 mL-agate jars, stoichiometric amounts of the precursor materials (1 mol Na_2CO_3 and 3 mol TiO_2) were mixed using 5-agate balls (6 mm), keeping fixed balls-to- materials mass ratio. The milling was conducted at varied speeds (from 200 to 800 rpm) and duration as mentioned for each synthesized material. Then, the milled materials were transferred into ceramic crucible and calcined in a tube furnace at 800 °C (as determined from TGA analysis) at constant heating rate (5 °C min^{-1}) under air. The as-synthesized titanates were left to naturally cool down to room temperature (*ca.* 23 °C).

2.2. Characterization of the as-synthesized titanates

The calcination temperature of the milled TiO_2–Na_2CO_3 mixture was determined by thermogravimetric analyzer TGA 4000 from PerkinElmer. Few milligrams of the mixture were placed onto aluminum crucible and the temperature was scanned from 25 to 800 °C under N_2 environment at a heating rate of 5 °C min^{-1}. A scanning electron microscope (SEM) from FEI Nova NanoSEM equipped with an energy-dispersive X-ray (EDX) analyzer was used to determine the morphology and the elemental composition in the as-synthesized samples. A small amount of freshly prepared sample was mounted on aluminum stub using conductive tape. A Raman spectrometer from ThermoFisher Scientific (DXR) equipped with a microscope MPlan 50 × /0.25 BD were used to collect the spectra of the freshly prepared powders, excited by laser beam at constant wavelength (633 nm) and the lowest excitation power. The crystalline structure and purity of the as-synthesized materials were accomplished by X-ray diffraction (XRD) using Panalytical Empyrean X-ray diffractometer with Cu Kα radiation (wavelength = 1.5406 Å), operating at scan rate of 2° min^{-1}. The surface composition of the powders was investigated by X-ray photoelectron spectroscopy (XPS) from Kratos (AXIS Ultra DLD). The binding energies were calibrated using C 1s peak (284.6 eV) as the internal standard. The microstructure of as-synthesized materials was examined by transmission electron microscope TEM (JEOL 100 CX). Trace amounts of sodium titanates were dispersed in acetone in a bath sonication for few minutes then a drop of the prepared dispersion was dried on grid of copper before characterization.

3. Results and discussion

3.1. Characterization of precursor materials and conditions

First, the structure and purity of precursor materials (TiO_2 anatase and anhydrous Na_2CO_3) have firstly investigated by Raman spectroscopy and X-ray diffraction (XRD). Raman scattering spectroscopy is very sensitive technique that locally probe the crystallinity and microstructures of materials. It relies on the vibrational motion of atoms in the unit cell and grains. Therefore, the synthesis of sodium titanate can be probed through investigating the change in Raman spectra due to the transformation of TiO_2 anatase (tetragonal structure) into targeted sodium titanates (mainly $Na_2Ti_3O_7$ or $Na_2Ti_6O_{13}$; monoclinic structures). Fig. 1a demonstrates the Raman spectra of the starting materials; TiO_2 anatase and Na_2CO_3. The spectrum of TiO_2 is dominated by five active Raman modes at 140, 192, 392, 512, and 635 cm^{-1}, which are characteristic for highly crystalline TiO_2 anatase, and consistent with the reported Raman scattering modes for similar material [3,41]. The strong Raman peak at 140 cm^{-1}, and the two bands at 192 and 635 cm^{-1} correspond to three E_g modes, which mainly are due to symmetric stretching vibration of O–Ti–O in TiO_2 [42]. The band at 512 cm^{-1} is a doublet of A_{1g} and B_{1g} modes, which is well resolved at low temperature [43]. These are, respectively, caused by antisymmetric and symmetric bending vibrations of O–Ti–O [42]. On the other hand, the crystalline Na_2CO_3 shows featured Raman active modes with weak bands at 182 and 696 cm^{-1}, and strong peak at 1075 cm^{-1} (inset of Fig. 1a), in agreement with those reported for anhydrous material [44].

X-ray diffraction reveals the long-range order of materials and gives structural information within several unit cells (grain), and hence the materials purity can be examined. Fig. 1b presents the patterns of TiO_2 anatase and anhydrous Na_2CO_3 and the reference diffraction lines with respect to tetragonal TiO_2 ($I4_1/amd$) and monoclinic ($C2/m$) lattices, respectively. As can be seen, TiO_2 is purely anatase phase with the usual tetragonal crystal structure characterized by rational intensities and positions of diffraction peaks at 2θ = 25.3° (011), 36.9° (013), 37.8° (003), 38.5° (112), 48.0° (020), 53.8° (015), 55.0° (121), 62.7° (024), 68.7° (116), and 70.3° (220) in good accordance with the diffraction peaks for TiO_2 anatase structure [45]. The anhydrous Na_2CO_3 used in this study is a mixture of γ– and β–forms, with highest proportion of γ–Na_2CO_3 as revealed from its pattern and corresponding reference lines (ICDD: 98-009-5549). Other prominent diffraction lines at 2θ = 33.9° (11–2) and 36.7° (310) are featured for β– Na_2CO_3 (ICDD:98-008-0999; lines are not shown in Fig. 1b).

3.2. Formation of metastable coarsen state under milling

Dry ball milling is a kind of mechanochemical synthesis (MCS) in which the reacting materials are exposed to milling energy that may be sufficient for the reaction completion and the formation of final product or just mechanically activates the reactants. The mechanical activation greatly enhances the reactivity of materials through various kinds of milling-induced physical changes such as grain refinement, defects and the lattice distortion, amorphization, and even formation of metastable polymorphs [46–49]. The input milling energy depends on the milling conditions and factors including milling speed and time, ball number and diameter, powder-to-ball mass ratio, and other instrumental factors [37,49–51]. The impact of milling energy (namely; cumulative milling energy E_{cum} in J g^{-1}) can be calculated from the phenomenological equations (Eqs. 1–3) [37,50] as detailed in the Supplementary Data, and summarized in Table S2, where the only two variables are the milling speed and time, and other milling parameters are constant. Henceforth, the impact of milling on the behavior of materials is alternatively represented either by the milling speed and time or the calculated milling energy (E_{cum}).

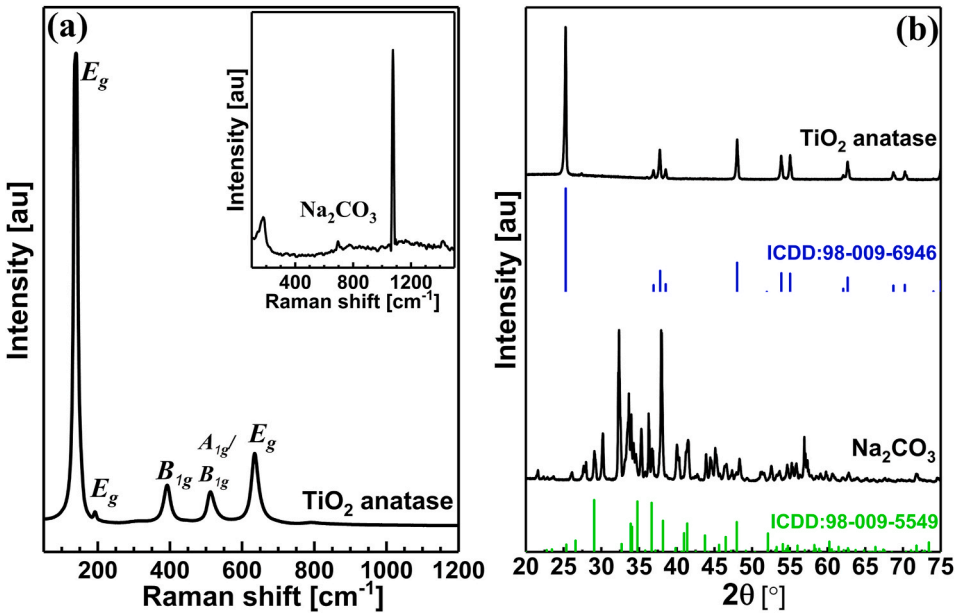

Fig. 1. (a) Raman spectra, and (b) XRD diffraction patterns of TiO_2 anatase and anhydrous Na_2CO_3 and their corresponding reference diffraction lines: ICDD: 98-015-6838 and ICDD: 98-009-5549, respectively.

First, to explore whether the input milling energy is sufficient to form the target sodium titanates or even distort the crystalline structure of starting materials, precursor materials have been mixed and examined before calcination. Fig. 1S presents the full XRD patterns of TiO_2–Na_2CO_3 mixtures milled at low (200 rpm) and high (800 rpm) speeds at varied milling durations. It can be seen that the mixtures show dominant reflections of TiO_2 anatase and weak peaks of Na_2CO_3 even at high milling energies. The Raman spectra of the mixtures resemble that

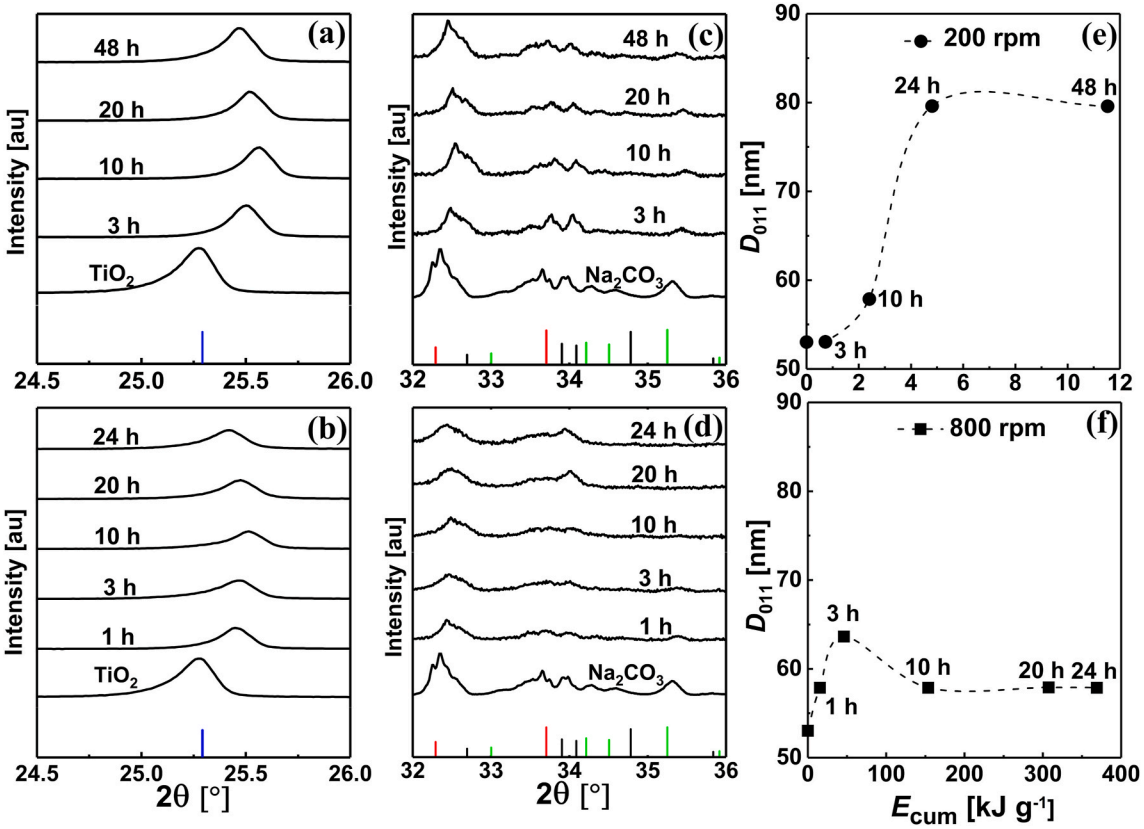

Fig. 2. Magnified XRD diffraction patterns of samples milled for different durations (from 1 h to 48 h) at (a, c) 200 rpm and (b, d) 800 rpm before calcination, and the variation of crystallite size D of TiO_2 with cumulative milling energy (E_{cum}) at 200 rpm (e) and 800 rpm (f). The patterns of TiO_2 and Na_2CO_3 are for unmilled samples. The reference diffraction lines for TiO_2 anatase (blue lines; ICDD: 98-009-6946), γ–Na_2CO_3 (green lines, ICDD: 98-009-5549), β– Na_2CO_3 (black lines, ICDD: 98-009-5549), and Na_2O (red lines, ICDD: 98-008-7179) are shown. The calculations of D_{011} based on Scherrer equation [53,54] are detailed in the Supplementary Data. (For interpretation of the references to colour in this figure legend, the reader is referred to the Web version of this article.)

of unmilled TiO_2 anatase and do not show any significant change, rather than a decrease in band intensities with prolonged milling (data not shown). This implies that the milling energy are not sufficient to produce the sodium titanates, and does not induce a phase transition in contrast with previous studies [47,48,52] that reported milling-induced polymorphic transformations of TiO_2 anatase. The existence of Na_2CO_3 is likely to suppress this polymorphic transition, which is sensitive to the environment [45].

Fig. 2(a and b) represent the magnified diffraction patterns in the small-angle regime that show the characteristic (011) reflection of TiO_2 anatase at $2\theta = 25.3^\circ$ in the mixtures milled at 200 and 800 rpm for varied durations. In both cases, the peak slightly shifts to smaller angles as the milling time increases until 10 h. This is likely to be a critical time beyond which the peak returns to slightly higher angles as the milling time further extends. This shift is almost ascribed to the uniform strain (macrostrain) [55] that results from lattice imperfections induced by milling energy [56–60]. Moreover, the trend of peak broadening non-monotonically varies with the milling energy, which is directly related to the variation of crystallite sizes [35,39,46,61]. Rationally, the crystallite size of TiO_2 in mixtures milled at high milling energy (800 rpm) is lower than those milled at lower energy (200 rpm) as evident from the peak intensities (Fig. 2a and b) and the dependency of crystallite sizes (D_{011}) with milling energy (Fig. 2e and f). As depicted in Fig. 2e, the crystallite size of TiO_2 in the mixtures milled at 200 rpm slightly increases until 10 h beyond which it suddenly increases before stabilizing at 20 h. Comparatively, the mixtures milled at higher energy (800 rpm) have smaller crystallite size than those milled at lower energy (200 rpm). As shown in Fig. 2f, D_{011} is in the range of *ac.* 60 nm (higher than that of unmilled TiO_2) over the milling energy range. Such extraordinarily increase of crystallite size upon milling has been rarely reported [62]. It may ascribes to the coarsening of mechanically activate titanates which tend to minimize the high surface energy through the oriented attachment mechanism [63]. Initially, the cumulative milling energy E_{cum} is insufficient to self-organize the new activated surfaces. Above a critical E_{cum} (*ca.* 2.5 kJ g^{-1}), the driving force for coarsening is achieved and the crystals grow and survive [64] over the range $E_{cum} \sim$ 4–12 kJ g^{-1} (Fig. 2e). At higher E_{cum}, the crystal growth is accompanied by long-range rearrangements; therefore, it would be kinetically suppressed [55]. Accordingly, the crystallite size of particles milled at 800 rpm are much smaller than those milled in the intermediate E_{cum} range. The milling energy does not alter the d_{011}-spacing that remains constant at ~3.50 nm that is the typical value of TiO_2 anatase. This indicates the milling does not promote the Na intercalation or induce polymorphic transition. In comparison to unmilled sample, the diffraction peaks of Na_2CO_3 (polymorphs) in the mixtures milled at 200 rpm are slightly less intense and shift to higher angles with time (Fig. 2c). The behavior is more pronounced at 800 rpm and the peak intensities strongly decrease so that the reflections at *ca.* 35.2° diminish upon further milling (Fig. 2d). This suggests that milling turns Na_2CO_3 to be amorphous.

In conclusion, the input milling energy are not sufficient for the reaction completion between TiO_2 and Na_2CO_3 and eventually the formation of sodium titanates. Instead, the reactants are mechanically activated where intermediate forms of coarsen (stacked) titanates is likely to form, pronouncedly at moderate cumulative milling energy (E_{cum} = 4–12 kJ g^{-1}). This amount of E_{cum} (7–12 kJ g^{-1}) was sufficient for the completion of a mechanochemical reaction of analogous mixture (Na_2CO_3 –Nb_2O_5) [38]. When Na_2CO_3 was replaced by K_2CO_3, an extremely higher E_{cum} (5200 kJ g^{-1}) was required for the product formation [35]. Rojac et al. systematically studied the rate of reaction between Na_2CO_3 and transition metal oxide [34]. It has been found that highly acidic metal cation reacts faster with Na_2CO_3, and the reaction proceeds through the formation of an amorphous carbonato complex (CO_3^{-2} anions coordinate to the transition metal cation) which decomposes upon further milling [34,35]. Due to instrumental limitation, we could not reach E_{cum} higher than ~730 kJ g^{-1}, which is still insufficient for the reaction completion.

To form the sodium titanates, the mechanically activated precursor materials is calcined at an exact temperature. The calcination temperature of an activated mixture was determined by thermogravimetric analysis (TGA), as shown in Fig. S2. The initial weight loss below 100 °C is about 2.0 wt%, which may corresponds to the desorption of water traces. In the temperature range of 440–710 °C, there is a considerable weight loss of about 14 wt% indicating that the evolution of CO_2 gas starts at about 440 °C. The strong peak at ca. 640 °C points out that the reaction between precursor materials occurs, according to the following chemical equation: $3TiO_2(s) + Na_2CO_3(s) \rightarrow Na_2Ti_3O_7(s) + CO_2(g)$. According to Tamman's rule, the reaction will only occur when the temperature reaches, at least, two-thirds of the melting point of one or more of the reactants [65]. The critical temperature of 640 °C is in accordance with this rule since the melting point of Na_2CO_3 is about 852 °C. Accordingly, the calcination temperature T = 800 °C was selected to ensure the reaction completion and avoid the formation of any possible phase transition. Previous reports have shown that longer calcination time is likely to be the cause of formation of polyphasic titanates in comparison to shorter time [1,22,32]. Accordingly, a short calcination time (3 h) has been used in this study.

3.3. Tunnel $Na_2Ti_6O_{13}$ vs layered $Na_2Ti_3O_7$ phases: the effect of milling speed

The TiO_2–Na_2CO_3 mixtures, milled at different speed and duration, were calcined under the same conditions: 800 °C for 3 h in air. In order to elucidate the impact of milling speed on the crystalline structure and type of sodium titanates, Raman spectra of the as-synthesized materials are depicted in Fig. 3. At a glance, the spectra are completely different from those of uncalcined mixtures, implying that new products are formed. The sample prepared at 200 rpm uniquely presents a spectrum that differs from those of samples prepared at higher milling speeds (Fig. 3). Its Raman spectrum perfectly coincides with that represented by the tunnel phase of sodium hexatitanate; $Na_2Ti_6O_{13}$ [66] where it is

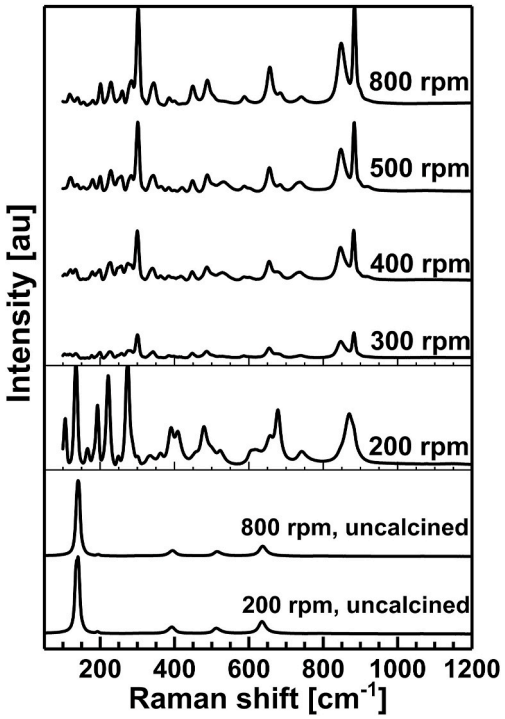

Fig. 3. Raman spectra of the as-synthesized sodium titanates prepared at different milling speeds (from 200 to 800 rpm) for 3 h at constant calcination conditions (800 °C for 3 h in air). Spectra of TiO_2–Na_2CO_3 mixtures milled at 200 and 800 rpm without calcination are shown.

dominated by strong, well-resolved peaks in the low-frequency regime (200–300 cm^{-1}), and weak/intermediate bands and doublets in the high-frequency regime (400–950 cm^{-1}). The same spectrum with rational peaks' intensity and frequency range has been reported in previous research for hexatitanates prepared by solid-state reaction [67–69], and hydrothermal [29] methods. However, $Na_2Ti_6O_{13}$ samples synthesized by hydrothermal method showed somewhat different (bands shape and frequency) Raman spectra [24,70]. The low-frequency Raman modes at about 198, 227 and 280 cm^{-1} correspond to the Na–O–Ti bonds [67]. The bands at 663 and 683 cm^{-1} are attributed to Ti–O–Ti stretching vibration in edge-shared TiO_6, whereas the band at 874 cm^{-1} is due to distorted TiO_6 with short Ti–O bond [67]. In comparison to the $Na_2Ti_6O_{13}$ prepared by hydrothermal method [24,70], no peak was detected above 1000 cm^{-1}, indicating the absence of any unreacted Na_2CO_3.

Interestingly, the samples prepared at higher milling speeds (≥300 rpm) show distinct spectra that are different from that of hexatitanate, implying that new phase is formed at higher milling speeds (Fig. 3). As the milling speed raises, the bands become more intense due to a presumable development of textured microstructure of nanorods that are roughly parallel to each other [24], as detailed below. The featured Raman spectra of the samples prepared at milling speeds ≥300 rpm identically match the spectra of layered $Na_2Ti_3O_7$ as reported in previous studies [66,68,71,72]. In contrast to the spectrum of $Na_2Ti_6O_{13}$, the low-frequency bands are very weak implying the restricted vibrational motions of Na atoms due to the zigzag structure of $Na_2Ti_3O_7$ [67]. The Raman modes at about 300, 340, 448, 654, 847 and 882 cm^{-1} are featured for layered $Na_2Ti_3O_7$ structure, and are assigned to stretching vibrations of Ti–O bonds [73].

In terms of crystalline structure, both layered $Na_2Ti_3O_7$ and tunnel $Na_2Ti_6O_{13}$ structures commonly have a monoclinic structure with two different symmetries ($P2_1/m$ and $C2/m$, respectively) and sets of lattice parameters, hence each phase certainly has a characteristic diffraction pattern. Fig. 4 depicts the XRD patterns of the as-synthesized samples and reference patterns of $Na_2Ti_6O_{13}$ and $Na_2Ti_3O_7$. First, no diffractions of unreacted starting materials have been detected, implying the reaction completion after calcination. The sample prepared at 200 rpm presents a diffraction pattern that is strikingly different from those of the samples prepared at higher speeds. This is consistent with Raman spectrum (Fig. 3), revealing that the type of titanates is sensitive to the mechanical activation of starting materials in their milled mixtures. As shown in Fig. 4, the powder diffraction pattern of the sample prepared at 200 rpm is uniquely consistent with the pattern of a reference $Na_2Ti_6O_{13}$ (ICDD:98-018-6996) with characteristic peaks being observed at $2\theta =$ 11.8° (200), 14.1° (20–1), 24.5° (110), 29.8° (310), 33.3° (402), 35.9° (60–1), 37.9° (11–3), 44.2° (602), and 48.5° (020). This is in good accordance with the diffraction patterns of $Na_2Ti_6O_{13}$ structure as reported in previous studies [3,5,10,18,30,74,75]. The calculated d_{200}-spacing ~0.75 nm that is characteristic for tunnel structure [10,29,76,77]. Additional peaks are detected at $2\theta = 10.5°$ and 15.9° which are characteristic for the less crystalline $Na_2T_3O_7$ phase. This indicates that the sample prepared at 200 rpm is a mixture of $Na_2Ti_6O_{13}$ and $Na_2T_3O_7$ phases, with relatively higher content of $Na_2Ti_6O_{13}$ phase.

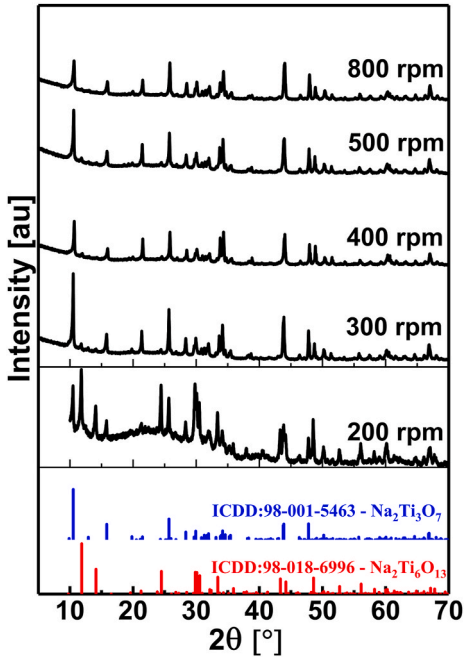

Fig. 4. XRD patterns of the as-synthesized sodium titanate samples prepared at different milling speeds (200–800 rpm) for 3 h at constant calcination conditions (800 °C for 3 h in air). The lines are the reference diffraction lines for $Na_2Ti_6O_{13}$ (ICDD:98-018-6996) and $Na_2Ti_3O_7$ (ICDD:98-001-5463).

The samples prepared at higher milling speeds (≥300 rpm) show powder diffraction patterns with identical peak positions and decreased intensities as the milling speed raises (Fig. 4). The patterns are consistent with that of a reference $Na_2T_3O_7$ (ICDD: 98-001-5463) with characteristic peaks being observed at $2\theta = 10.5°$ (100), 15.8° (101), 21.4° (201), 25.7° (110), 28.4° (111), 30.0° (003), 34.2° (302), and 43.9° (104). Similar diffraction patterns have been reported for $Na_2T_3O_7$ nanorods prepared by hydrothermal [10,24,28], and solid-state [14,31,32,78] methods. It is worth noting that $Na_2T_3O_7$ phase is dominant as revealed from the consistency of its Bragg peaks and the corresponding reference ones, and the d_{100}-spacing of 0.84 nm that delineate the layered structure [77]. The coexistence of trace amounts of $Na_2T_6O_{13}$ is evident from the weak peaks at 11.8°, which nearly disappear at higher speed (800 rpm) (Fig. 4). In addition, the change of the intensity of peaks with milling speed is likely to attribute to variation of particle size as will be confirmed by SEM analysis. Obviously, the structure and purity of phases are sensitive to the milling energy where $Na_2T_3O_7$ phase favorably dominates at higher milling energy. The coexistence of the two crystalline structures have been previously reported for sodium titanates synthesized by hydrothermal [9,10,24,30,70,72,75], wet-milling [32], and stirring [75] methods, where it has been shown to be sensitive to the synthesis conditions and calcination temperature [13,25,70].

The surface oxidation state and composition of constituent elements of the as-synthesized titanates can be determined by X-ray photoelectron spectroscopy (XPS). Fig. 5 depicts the typical survey and high-resolution XPS spectra for samples synthesized at different milling speeds. The survey spectra disclose the existence of symmetric peaks for Ti, O, Na and C elements in the powders (Fig. 5a). The weak peak of carbon is mainly an instrumental contribution due to the contamination by hydrocarbons [79]. The high-resolution spectra of Ti (2p) show two photoelectron peaks centered at binding energies of 458.8 eV and 464.7 eV corresponding to the Ti $2p_{3/2}$ and Ti $2p_{1/2}$, respectively (Fig. 5b). These energies are characteristic for Ti^{4+} state of TiO_2 [79,80], and have been shown in analogous sodium titanates [23,81–84]. As shown in Fig. 5c, the binding energy at 1071.9 eV is characteristic for Na 1s [85] and assigned to Na–O bond of sodium titanates [14,84,86]. The photoemission peak of O 1s centered at 530.4 eV (Fig. 5d) is evident for O–Ti bond [84,86], which extends to higher binding energies (532–534 eV) due to likely unreacted carbonates [87]. Qualitatively, XPS peak positions cannot clearly differentiate between $Na_2Ti_3O_7$ and $Na_2Ti_6O_{13}$ phases and any variation in peaks shape or position (binding energies) is associated with sample preparation and conditions, and presumably instrumental parameters [88]. Nevertheless, the sample synthesized at 200 rpm clearly shows more intense (Ti, Na, and O) peaks than those for samples synthesized at higher milling speeds (Fig. 5b–d).

Quantitatively, the atomic percentages of constituent elements (Na, Ti, O) are calculated from the area under each corresponding peak, as shown in Table S3. The sample prepared at 200 rpm shows lower oxygen content and higher Na:Ti ratio (~0.48) than that of reference $Na_2Ti_6O_{13}$

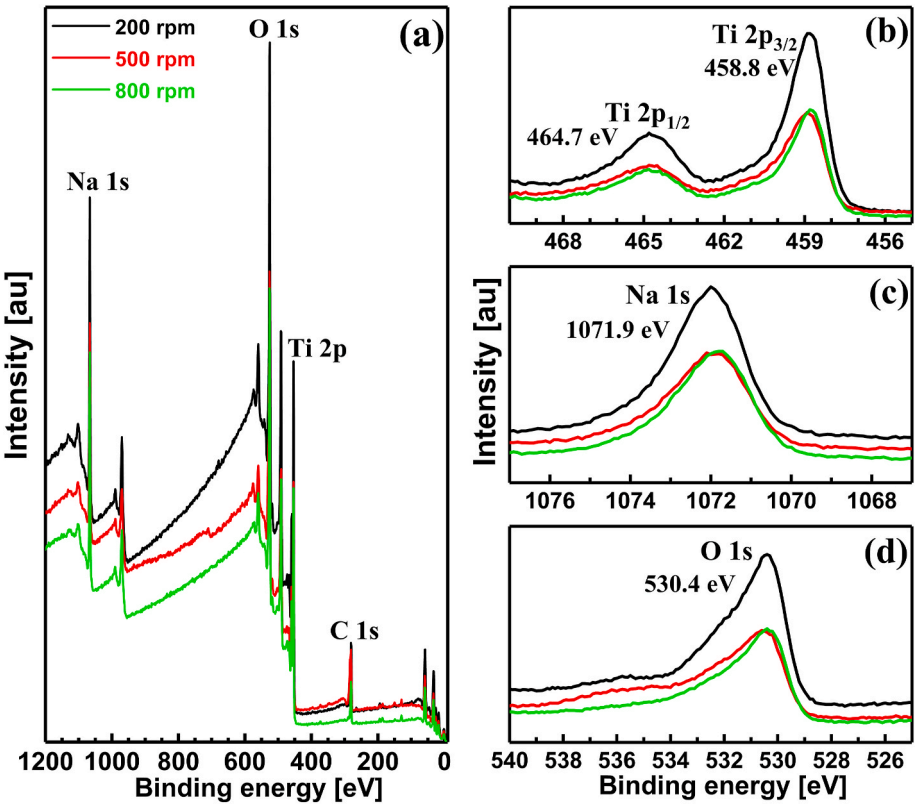

Fig. 5. (a) XPS survey spectra, and high-resolution spectra of (b) Ti 2p, (c) Na 1s, and (d) O 1s of samples prepared at 200, 500 and 800 rpm for 3 h, calcined at 800 °C for 3 h in air.

(~0.36) implying that the surface is rich in sodium [19,29,69]. In contrary, the surface of samples prepared at higher speeds (500 and 800 rpm) is Na-deficient as indicated from the low Na:Ti ratios (~0.53, 0.56) in comparison to the reference $Na_2Ti_3O_7$ (~0.67) (Table S3). In order to better confirm the elemental composition in the bulk of the as-synthesized samples, energy dispersive X-ray spectra (EDX) are collected as shown in Fig. S3 and summarized in Table S3. The Na:Ti ratio (~0.45) of the sample prepared at 200 rpm remains higher than that of reference $Na_2Ti_6O_{13}$, which may be related to the coexistence of the two phases as revealed from XRD analysis (Fig. 4). However, the samples prepared at higher milling speeds show comparable Na:Ti ratio (~0.71) to that of reference $Na_2Ti_3O_7$. Obviously, the sample prepared at higher milling speeds are dominate by $Na_2Ti_3O_7$ phase, while that prepared at lower speeds (200 rpm) is mainly composed of the two forms of sodium titanate ($Na_2Ti_6O_{13}$ and $Na_2Ti_3O_7$).

Fig. 6 presents the SEM micrographs for samples prepared at different milling speeds, under the same conditions as described in the figure caption. In general, the as-synthesized materials are homogenously dispersed and no agglomerations are observed in contrast to the materials synthesized by hydrothermal method [21,26,89]. As shown in Fig. 6a, the sample prepared at 200 rpm dominantly has a cuboid-like morphology with low-aspect ratio and an approximate size of *ca.* 120–300 nm in width and *ca.* 250–500 nm in length. Trace of short nanorods having nearly the same width and slightly longer than cuboids is overserved. As the milling speed increases, the nanorods morphology dominates with existence of some cuboid-like structures. At 300 rpm, the sample has relatively short nanorods with dimensions of *ca.* 120–400 nm in width and *ca.* 700 nm–1.0 μm in length (Fig. 6b). The elevated milling speeds enhance the longitudinal growth of nanorods without considerable change in the width, so that the nanorods have length of *ca.* 700 nm–1.1 μm at 500 rpm (Fig. 6c) and *ca.* 850 nm–1.4 μm at 800 rpm (Fig. 6d). It is worth noting that the input milling energy controls the morphology of titanates. Recall the analysis of Raman and XRD, hexatitnates are dominant at low milling energy (200 rpm), while trititanates do at higher energies (≤300 rpm). It seems accordingly that this crystalline transformation is linked with the change in the morphology from cuboids to nanorods. Thus, the cuboid-like particles are $Na_2Ti_6O_{13}$, whilst the $Na_2Ti_3O_7$ has nanorod-like morphology with higher aspect ratio where it dominates at higher milling energy. According to a significant amount of research, there is no unified morphology for either $Na_2Ti_6O_{13}$ or $Na_2Ti_3O_7$. The unpredicted morphology is likely to be sensitive to the synthesis method (commonly hydrothermal and solid-state), and conditions (starting materials, reaction duration, calcination temperature, etc.). For instance, solid-state method produced $Na_2Ti_3O_7$ nanoribbons [1], nanosheets [14], or nanoplates [78] using the same starting materials (TiO_2 anatase and Na_2CO_3) and calcination temperature (800 °C). The same method and conditions yielded $Na_2Ti_6O_{13}$ aggregates [90] and nanofibers [11,22]. It should be stated that the solid-state method somewhat resembles the mechanochemical method, however, the input activation energy of the former is uncontrollable and hence we observe variation in the morphology sodium titanates. In consistent with our findings, the hydrothermal method produced $Na_2Ti_6O_{13}$ with cuboid-like [26] and nanofiber [9] morphology.

The microstructure of the as-synthesized sodium titanates was further investigated by transmission electron microscopy (TEM). Figures S4a,b showed TEM micrographs for the samples prepared at 200 and 800 rpm. The sample prepared at 200 rpm has cuboid-like morphology (Fig. S4a) characteristic for $Na_2Ti_6O_{13}$, while longer $Na_2Ti_3O_7$ nanorods are formed at 800 rpm (Fig. S4b). Figure S4c presents the selected area electron diffraction (SAED) pattern of the sample prepared at 200 rpm ($Na_2Ti_6O_{13}$) which exhibited a monoclinic characteristic spot pattern and proved that the phase was single crystalline. Its high-resolution TEM (HRTEM) images provided a set of clear lattice fringes of $Na_2Ti_6O_{13}$ (Fig. S4e). The SAED image of the sample prepared at 800 rpm (Fig. S4d) clearly indicates the single–crystal nature with

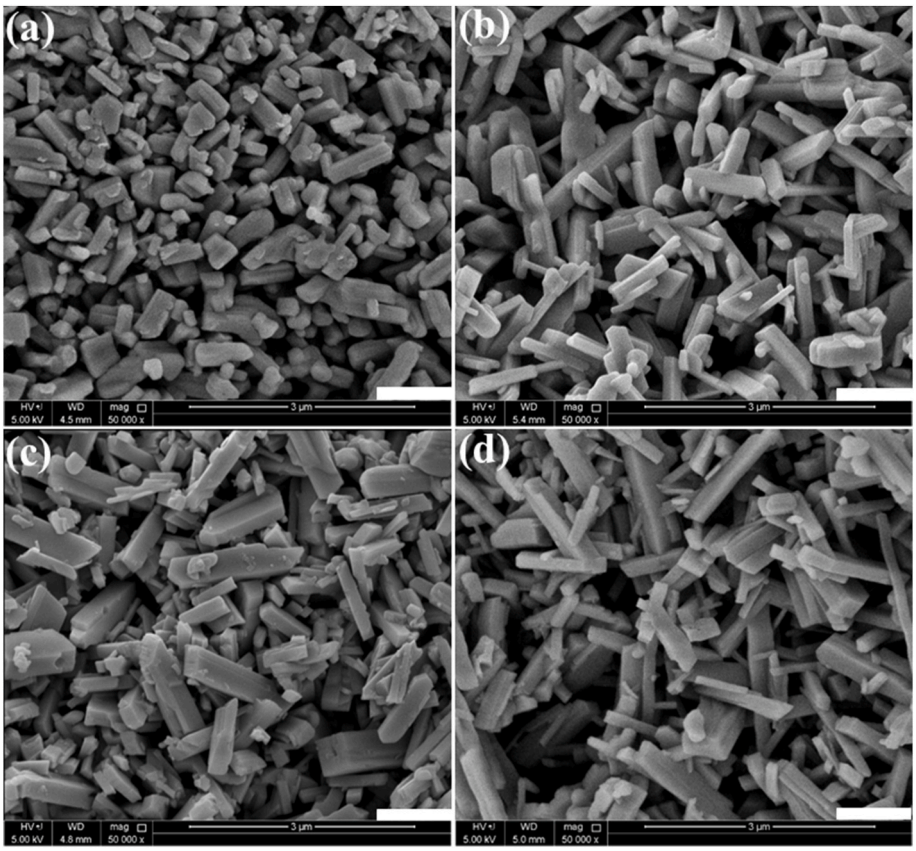

Fig. 6. SEM micrographs of the as-synthesized sodium titanate samples prepared at different milling speeds (a) 200 rpm, (b) 300 rpm, (c) 500 rpm, and (d) 800 rpm for 3 h at constant calcination conditions (800 °C for 3 h in air). The scale bar corresponds to 1 μm.

preferential growth along [010] direction revealing the layered structure of $Na_2Ti_3O_7$. The HRTEM image displays defect–free highly crystalline layered structure with interplanar spacing of *ca.* 8.0 Å corresponding to (200) plane.

3.4. Effect of milling time

So far, the effect of cumulative milling energy (E_{cum}) at constant milling time (3 h) has been explored. It has been concluded that $Na_2Ti_6O_{13}$ and $Na_2Ti_3O_7$ are dominantly existed at low (200 rpm) and high (300–800 rpm) milling speed, respectively, with trace amounts of other phase. Now, it is worth to investigate the effect of milling time at constant speed to accurately investigate the influence of ball-impact energy (ΔE_b) on the crystalline structure and purity of titanates.

Fig. 7 demonstrates the effect of milling duration on the crystallinity and purity, represented by Raman spectra and XRD patterns, of sodium titanates synthesized at 200 rpm. Obviously, the samples synthesized by milling for a duration of 3–20 h show nearly identical Raman spectra featured for $Na_2Ti_6O_{13}$ phase (Fig. 7a). However, the band at 275 cm^{-1}, corresponding to Na–O–Ti bond [70], slightly shifts to lower frequency. This redshift is likely to be consistent with the increasing of the Ti–O bond length, which signifies the transformation of $Na_2Ti_3O_7$ (short Ti–O bond length ~ 0.17 nm) into $Na_2Ti_6O_{13}$ (long Ti–O bond length ~ 0.22 nm) [70] as the milling time increases. In previous studies, sodium titanates exhibited similar [68,70] and opposite [72] phase transition depending on the synthesis method and its conditions. The sample milled at prolonged time of 24 h surprisingly shows a Raman spectrum that clearly corresponds to neither pure structure of $Na_2Ti_6O_{13}$ nor $Na_2Ti_3O_7$ (Fig. 7b). Indeed, the spectrum has some features from both phases with high-frequency peaks characteristic for $Na_2Ti_3O_7$ and low-frequency ones of $Na_2Ti_6O_{13}$ structure. The unusual intense doublet at 275 and 303 cm^{-1} (assigned to Na–O–Ti bond vibration) and peak at 883 cm^{-1} (assigned to short Ti–O bond vibration) may indicate a formation of an intermediate pseudo-tunnel phase [72] in which sodium bridges result in compact TiO_6 octahedra. The sample synthesized at prolonged milling for 48 h clearly presents a Raman spectrum characteristic for $Na_2Ti_3O_7$ phase.

XRD patterns (Fig. 7b) reveal a coexistence of the two phases in the samples prepared at 200 rpm with dominant $Na_2Ti_6O_{13}$ phase. As the milling time increases from 3 to 20 h, the relative intensities of diffraction peaks of $Na_2Ti_6O_{13}$ notably increase on the expenses of drop in the intensities of characteristic peaks of $Na_2Ti_3O_7$ phase (labelled by red arrows in Fig. 7b), so that the sample milled for 20 h are dominated by $Na_2Ti_6O_{13}$ phase with minor traces of other phase. This observation supports the conclusion withdrew from Raman data where the prolonged milling time at 200 rpm seems to favorably form the tunnel phase. The 20 h is likely to be a critical milling time beyond which the diffraction peaks of $Na_2Ti_3O_7$ become more intense than those correspond to $Na_2Ti_6O_{13}$ phase at 24 h (Fig. 7b). Indeed, the sample milled for 24 h shows diffraction peaks of mixed phases but its Raman spectrum (Fig. 7a) manifests an intermediate structure. Several studies [29,70,72] have reported this intermediate phase without clear identification for its structure due to inconsistent Raman modes and unindexed diffractions. Further prolonged milling for 48 h produces an almost pure $Na_2Ti_3O_7$ phase as evident from the diminishing of the reflections of $Na_2Ti_6O_{13}$ phase.

The gradual morphological change of the as-synthesized samples upon prolonged milling at 200 rpm is depicted in the SEM micrographs in Fig. 8 a-c. Initially, the sample synthesized at 200 rpm for 3 h has a cuboid-like morphology with average width of *ca.* 210 nm and length of *ca.* 375 nm (Fig. 8a). As the milling time increased to 5 h, the sample still has the same morphology with increase in the average width (*ca.* 300

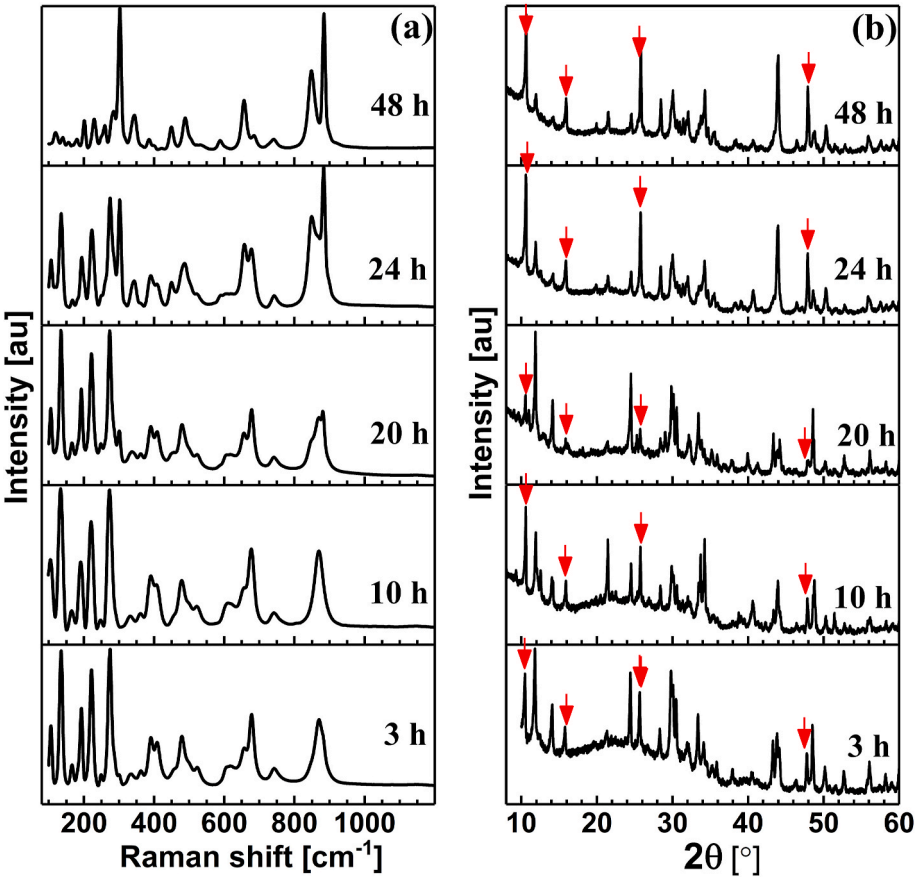

Fig. 7. Raman spectra (a) and XRD diffraction patterns (b) for samples prepared at 200 rpm at varied milling time from 3 h to 48 h, under the same calcination conditions (800 °C for 3 h in air). The red arrows correspond to the characteristic peaks of $Na_2Ti_3O_7$ phase. (For interpretation of the references to colour in this figure legend, the reader is referred to the Web version of this article.)

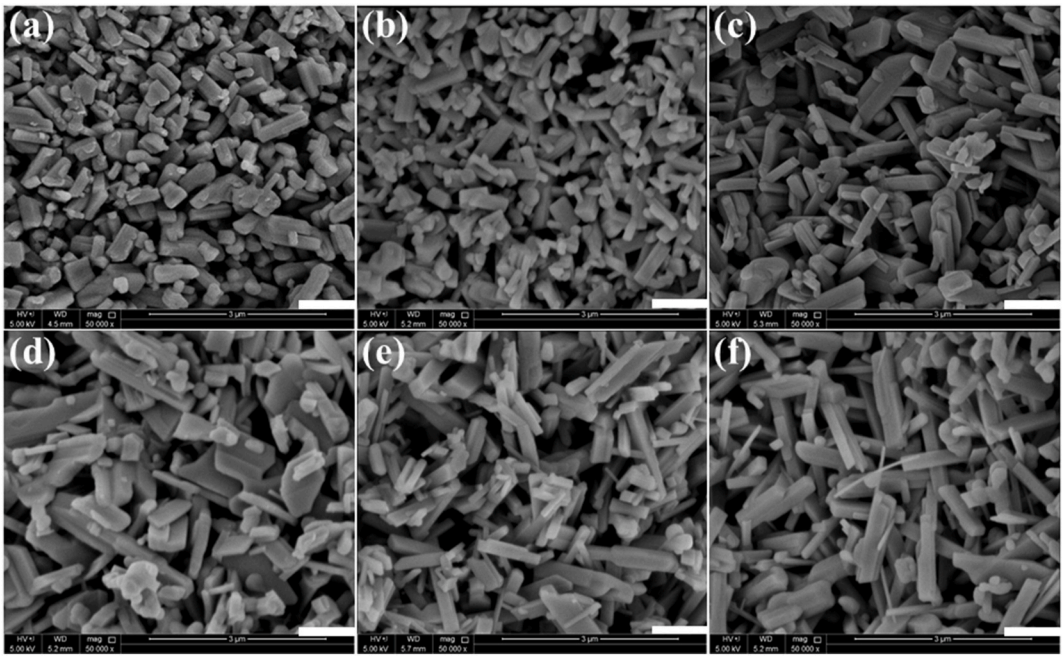

Fig. 8. SEM micrographs of the as-synthesized sodium titanates showing the effect of milling time at two different speeds; 200 rpm ((a) 3 h, (b) 5 h, (c) 48 h) and 800 rpm ((d) 1 h, (e) 5 h, (f) 10 h) at constant calcination conditions (800 °C for 3 h in air). The scale bar corresponds to 1 μm.

nm) and length (*ca.* 650 nm) (Fig. 8b). As revealed from XRD data, the sample milled at 3 h is an $Na_2Ti_6O_{13}$–dominant mixture of the two phases. Prolonged milling for 48 h results in a homogenously distributed nanorods with average width of *ca.* 265 nm and length of *ca.* 750 nm (Fig. 8c). This morphological change from short cuboid-like structures to longer nanorods is likely to be consistent with the phase transformation from $Na_2Ti_6O_{13}$ to $Na_2Ti_3O_7$.

The effect of milling time at high milling speed (800 rpm) on the crystalline structure and purity of the as-synthesized titanates is depicted in Fig. 9. As revealed from Raman spectra, there is no structural change upon milling the sample for prolonged time at 800 rpm. The samples milled over a duration from 3 to 20 h show Raman spectra characteristic for $Na_2Ti_3O_7$ structure (Fig. 9a). However, the Raman spectrum of the sample milled at shorter time (1 h) is not associated with that of a pure titanate phase having a mixture of bands characteristic for $Na_2Ti_3O_7$ (at high frequency) and $Na_2Ti_6O_{13}$ (at low frequency). Nevertheless, the XRD patterns do not show any significant change over milling duration from 1 to 20 h, where the samples have identical diffraction patterns of a pure $Na_2Ti_3O_7$ phase (Fig. 9b). Moreover, no peaks from precursor materials are observed, and hence prolonged milling does not decompose the titanates. The sole change upon prolonged milling at 800 rpm is the variation of the diffraction intensity, where the sample milled for 5 h exhibits the most intense peaks implying that the highest crystallinity is achieved under this condition.

Interestingly, the morphology of the sample synthesized at 800 rpm for 1 h is submicron platelet-like structures (Fig. 8d). The nanorods begin to appear in the sample milled for 3 h (Fig. 6d), which longitudinally grow with the samples prepared at prolonged milling durations without significant change in the width. The sample synthesized at 800 rpm for 5 h shows an average length of *ca.* 750 nm (Fig. 8e), which increases to *ca.* 1.4 μm with the sample milled for 10 h (Fig. 8f).

4. Discussion

The mechanochemical reaction reaches a completion when the cumulative milling energy (E_{cum}) exceeds the energy barrier (activation energy) and eventually the final product is formed [46,49]. The high milling energy (E_{cum} ~ 730 kJ g^{-1}) and presumable temperature of milling (*ca.* 200 °C [91]) are not the necessary conditions for a complete mechanochemical reaction between TiO_2 anatase and Na_2CO_3 and formation of sodium titanates as suggested from XRD patterns (Figs S1). Obviously, the calcination (at 800 °C, as revealed from TGA analysis) of the mechanically mixed reactants urges the production of titanates. Interestingly, the formation of the most common phases; $Na_2Ti_3O_7$ and $Na_2Ti_6O_{13}$ of titanates is more sensitive to the mechanical activation applied before calcination, rather than the stoichiometric ratio of reactants. This is likely to be the significance of the input milling energy that results in variety of physical transformations in the reactants such as formation of new surfaces, defects and the lattice distortion, amorphization, and even formation of metastable polymorphs [46–48]. No polymorphic transformation of TiO_2 anatase has been observed, presumably due to the milling environment (presence of Na_2CO_3) in accordance with previous study [33]. Instead, the TiO_2 is mechanically exfoliated to titanate nanosheets [89]. These energetic nanosheets tend to coarsen [63] and stack to eventually form a metastable thick coarsen phase that survive at low milling speed (200 rpm). Different metastable phase seems to form at higher milling speeds (≥300 rpm), when the high energy suppresses the stacking of nanosheets and the splitting growth mechanism [92] drives the formation of relatively long and thin metastable phase. While the amorphization of Na_2CO_3 simply increases as the milling speed raises (Fig. 2c and d), the type of metastable phase is more sensitive to the ball-impact energy (ΔE_b) rather than cumulative milling energy (E_{cum}). In general, stacked coarsen phase is predominant at low ΔE_b ~0.231 mJ hit^{-1} (i.e. 200 rpm), whereas longer metastable phase is favorable at higher ΔE_b ~0.519–3.69 mJ hit^{-1} (i.e. ≥300 rpm) as deduced from the variation of crystallite size with milling speed (Fig. 2e and f). (Detailed calculations for E_{cum} and ΔE_b and values are explained and tabulated in Table S2 in the Supplementary Data).

Considering the reaction is diffusion-controlled [93], the calcination decomposes the Na_2CO_3 at the interface and promotes the diffusion of

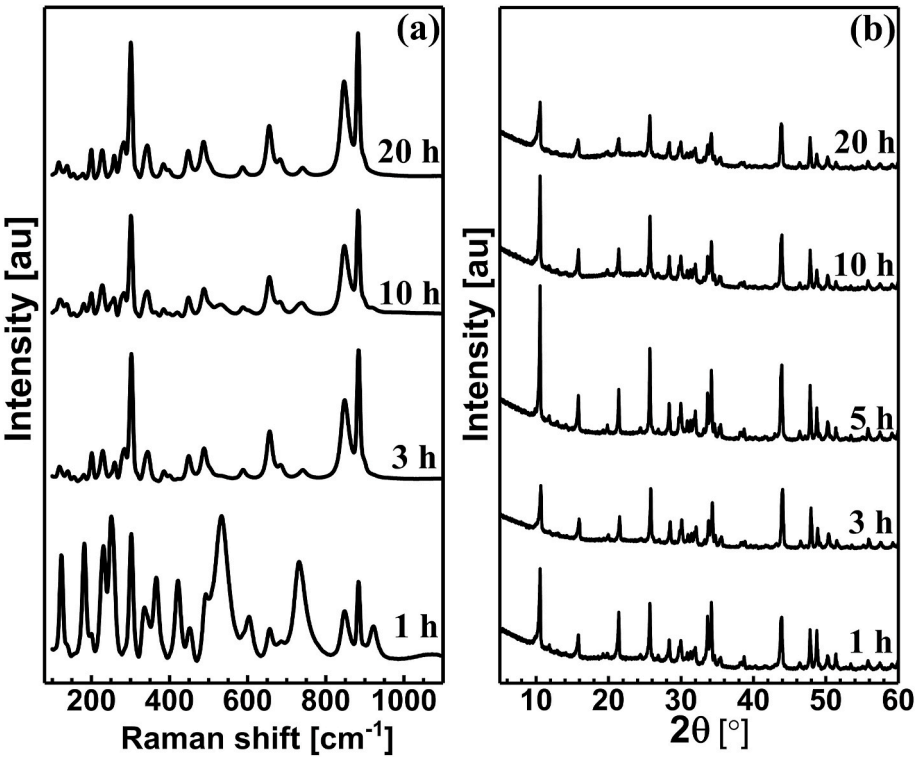

Fig. 9. Raman spectra (a) and XRD diffraction patterns (b) for samples prepared at 800 rpm at varied milling time from 3 h to 20 h, under the same calcination conditions (800 °C for 3 h in air).

Na^+ and O^{-2} ions into the interior of TiO_2 to finally produce $Na_2Ti_6O_{13}$ or $Na_2Ti_3O_7$ phase according to the nature of metastable phase. At low ball-impact energy (i.e. 200 rpm), the stacked metastable phase seems to have a tunnel network of polymerized TiO_6 octahedron [27] in which Na^+ ions diffuse to neutralize the charge of TiO_6 [94] during calcination and eventually form the tunnel $Na_2Ti_6O_{13}$ phase. This phase is thicker than $Na_2Ti_3O_7$ as revealed from SEM analysis (Fig. 6) and consistent with previous report [10]. A thin metastable phase is favorable at higher ball-impact energy (≥300 rpm), in which the TiO_6 octahedrons are connected through edges or corners [95] in longitudinally grown layered structures where Na^+ ions intercalate upon calcination, and the layered $Na_2Ti_3O_7$ structure is formed.

The Raman and XRD analysis (Figs. 3 and 4) differentiate two phases of sodium titanates; tunnel $Na_2Ti_6O_{13}$ and layered $Na_2Ti_3O_7$ structures formed, respectively, at low and high ball-impact energies. However, the coexistence of the two phases at low cumulative milling energy (i.e. 200 rpm, 3 h – Table S2) is pronounced as revealed from XRD (Fig. 3). This implies the significance of the milling time where 3 h was not sufficient to make the stacked coarsen phase dominate. At constant ΔE_b ~0.231 mJ hit^{-1} (i.e. 200 rpm), the crystallite size is significantly increases after 10 h (Fig. 2e), that is consistent with the gradual diminishing of the main reflections of $Na_2Ti_3O_7$ (at $2\theta = 10.5°$, 15.8°, 25.7°) until 20 h (Fig. 7b). This trend suggests that the 200 rpm–20 h is the optimal milling condition at which the stacked metastable phase is dominant and hence the tunnel $Na_2Ti_6O_{13}$ phase is dominant. Prolonged milling beyond 20 h is likely to turn the metastable phase more amorphous and hence a less crystalline $Na_2Ti_3O_7$ phase reappears. This behavior is in agreement with previous studies that highlighted the influence of milling time on the crystallinity [35,96]. At higher $\Delta E_b \geq 0.591$ mJ hit^{-1} (i.e. ≥300 rpm), the two metastable phases may coexist with domination of the less crystalline metastable phase (Fig. 2b). Upon calcination, the layered $Na_2Ti_3O_7$ obviously forms with coexistence of traces of the tunnel $Na_2Ti_6O_{13}$ as revealed from its very weak XRD peaks (Fig. 4). In this high ΔE_b limit, the cumulative milling energy seems merely to influence the crystallinity of $Na_2Ti_3O_7$ rather than any notable structural transitions. This is evident from the variation of Raman spectra and XRD patterns of samples prepared at 800 rpm (Figs. 9) and 400 rpm (Fig. S5) with milling time.

The milling energy influences the morphology of the as-synthesized titanates. The tunnel $Na_2Ti_6O_{13}$ phase is cuboid-like structure with lower aspect ratio than nanorods of the layered $Na_2Ti_3O_7$ phase (Figs. 6 and 8). The increased milling energy does not tremendously change the particle width. Both structures have a comparable average width in the range of *ca.* 200–300 nm. Nevertheless, the milling energy promotes a longitudinal growth of the particles. The layered $Na_2Ti_3O_7$ show a length in the range of *ca.* 900 nm–1.4 μm, whereas the tunnel $Na_2Ti_6O_{13}$ has shorter length in the range of *ca.* 375–750 nm.

5. Conclusion

The sodium titanates ($Na_2Ti_nO_{2n+1}$) have variety of unpredictable crystalline structures and morphology that is sensitive to the synthesis method and conditions. In this study, we demonstrated the efficacy of robust mechanochemical (dry ball milling) method to synthesis the most common phases; sodium trititanate ($Na_2Ti_3O_7$) and sodium hexatitanate ($Na_2Ti_6O_{13}$) without any undesired byproducts such as titanic acids. It has been found that the input milling energy mechanically activates the starting materials (TiO_2 anatase and Na_2CO_3) resulting in metastable phases that produce the sodium titanates after calcination. The cuboid-like $Na_2Ti_6O_{13}$ phase was favorably formed at low ball-impact energy (ΔE_b) that corresponds to 200 rpm, while the nanorod-like $Na_2Ti_3O_7$ is dominantly produced higher ΔE_b (i.e. ≥300 rpm) under constant milling (ball diameter and number, jar volume, etc) and calcination (800 °C, 3 h, in air) conditions, and the stoichiometric amounts of starting materials. The purity, crystallinity and morphology of sodium titanates are sensitive to the cumulative milling energy (E_{cum}), i.e. the milling time at particular ΔE_b (i.e. milling speed). At low ΔE_b, highly pure $Na_2Ti_6O_{13}$ was formed at 200 rpm for 20 h. Highly crystalline $Na_2Ti_3O_7$ was preferably produced at higher ΔE_b (i.e. ≥300 rpm) at a particular milling time that depends on the milling speed. The cuboid $Na_2Ti_6O_{13}$ and the nanorod $Na_2T_3O_7$ structures had nearly constant width (*ca.* 200–300), and longitudinally grew with the increased cumulative milling energy, reaching maximum length of *ca.* 900 nm–1.4 μm.

Declaration of competing interest

The authors declare that they have no known competing financial interests or personal relationships that could have appeared to influence the work reported in this paper.

Acknowledgment

This work was supported by Qatar University [Grant No. QUST-1-CAS-2019-16]. The authors would like to thank staff at the Central Laboratories Unit, Qatar University for accomplishing SEM, TEM and Raman spectroscopy, and the staff at the Center for Advanced Materials, Qatar University for performing the XRD measurements.

Appendix A. Supplementary data

Supplementary data to this article can be found online at https://doi.org/10.1016/j.ceramint.2021.01.271.

References

[1] P. Senguttuvan, G. Rousse, V. Seznec, J.-M. Tarascon, M.R. Palacín, $Na_2Ti_3O_7$: lowest voltage ever reported oxide insertion electrode for sodium ion batteries, Chem. Mater. 23 (18) (2011) 4109–4111, https://doi.org/10.1021/cm202076g.
[2] M.Á. Muñoz-Márquez, D. Saurel, J.L. Gómez-Cámer, M. Casas-Cabanas, E. Castillo-Martínez, T. Rojo, Na-ion batteries for large scale Applications: a review on anode materials and solid electrolyte interphase formation, Adv. Energy Mater. 7 (20) (2017) 1700463–1700493, https://doi.org/10.1002/aenm.201700463.
[3] D.C. Manfroi, A. dos Anjos, A.A. Cavalheiro, L.A. Perazolli, J.A. Varela, M. A. Zaghete, Titanate nanotubes produced from microwave-assisted hydrothermal synthesis: photocatalytic and structural properties, Ceram. Int. 40 (9) (2014) 14483–14491, https://doi.org/10.1016/j.ceramint.2014.07.007.
[4] Y.-C. Chang, J.-C. Lin, S.-H. Wu, One-step growth of $Na_2Ti_3O_7$ nanorods for enhanced photocatalytic activities and recyclability, J. Alloys Compd. 749 (2018) 955–960, https://doi.org/10.1016/j.jallcom.2018.03.332.
[5] J. Ramírez-Salgado, E. Djurado, P. Fabry, Synthesis of sodium titanate composites by sol-gel method for use in gas potentiometric sensors, J. Eur. Ceram. Soc. 24 (8) (2004) 2477–2483, https://doi.org/10.1016/j.jeurceramsoc.2003.07.014.
[6] C.-Y. Xu, J. Wu, P. Zhang, S.-P. Hu, J.-X. Cui, Z.-Q. Wang, Y.-D. Huang, L. Zhen, Molten salt synthesis of $Na_2Ti_3O_7$ and $Na_2Ti_6O_{13}$ one-dimensional nanostructures and their photocatalytic and humidity sensing properties, CrystEngComm 15 (17) (2013) 3448–3454, https://doi.org/10.1039/c3ce27092k.
[7] I. Becker, I. Hofmann, F.A. Müller, Preparation of bioactive sodium titanate ceramics, J. Eur. Ceram. Soc. 27 (16) (2007) 4547–4553, https://doi.org/10.1016/j.jeurceramsoc.2007.03.024.
[8] A. Rudola, K. Saravanan, S. Devaraj, H. Gong, P. Balaya, $Na_2Ti_6O_{13}$: a potential anode for grid-storage sodium-ion batteries, Chem. Commun. 49 (67) (2013) 7451–7453, https://doi.org/10.1039/c3cc44381g.
[9] O. Cech, K. Castkova, L. Chladil, P. Dohnal, P. Cudek, J. Libich, P. Vanysek, Synthesis and characterization of $Na_2Ti_6O_{13}$ and $Na_2Ti_6O_{13}/Na_2Ti_3O_7$ sodium titanates with nanorod-like structure as negative electrode materials for sodium-ion batteries, J. Energy Storage 14 (2017) 391–398, https://doi.org/10.1016/j.est.2017.07.008.
[10] C. Wu, W. Hua, Z. Zhang, B. Zhong, Z. Yang, G. Feng, W. Xiang, Z. Wu, X. Guo, Design and synthesis of layered $Na_2Ti_3O_7$ and tunnel $Na_2Ti_6O_{13}$ hybrid structures with enhanced electrochemical behavior for sodium-ion batteries, Adv. Sci. 5 (9) (2018) 1800519–1800526, https://doi.org/10.1002/advs.201800519.
[11] S. Chauque, C.B. Robledo, E.P.M. Leiva, F.Y. Oliva, O.R. Cámara, Comparative study of different alkali (Na, Li) titanate substrates as active materials for anodes of lithium - ion batteries, ECS Trans 63 (1) (2014) 113–128, https://doi.org/10.1149/06301.0113ecst.
[12] H. Zhang, G.R. Li, L.P. An, T.Y. Yan, X.P. Gao, H.Y. Zhu, Electrochemical lithium storage of titanate and titania nanotubes and nanorods, J. Phys. Chem. C 111 (16) (2007) 6143–6148, https://doi.org/10.1021/jp0702595.
[13] H. Zhang, X.P. Gao, G.R. Li, T.Y. Yan, H.Y. Zhu, Electrochemical lithium storage of sodium titanate nanotubes and nanorods, Electrochim. Acta 53 (24) (2008) 7061–7068, https://doi.org/10.1016/j.electacta.2008.05.036.
[14] J.S. Ko, V.V. Doan-Nguyen, H.S. Kim, G.A. Muller, A.C. Serino, P.S. Weiss, B. S. Dunn, $Na_2Ti_3O_7$ nanoplatelets and nanosheets derived from a modified

exfoliation process for use as a high-capacity sodium-ion negative electrode, ACS Appl. Mater. Interfaces 9 (2) (2017) 1416–1425, https://doi.org/10.1021/acsami.6b10790.
[15] P. Li, P. Wang, S. Qian, H. Yu, X. Lin, M. Shui, X. Zheng, N. Long, J. Shu, Synthesis of $Na_2Ti_6O_{13}$ nanorods as possible anode materials for rechargeable lithium ion batteries, Electrochim. Acta 187 (2016) 46–54, https://doi.org/10.1016/j.electacta.2015.11.057.
[16] H. Pan, X. Lu, X. Yu, Y.-S. Hu, H. Li, X.-Q. Yang, L. Chen, Sodium storage and transport properties in layered Na2Ti3O7 for room-temperature sodium-ion batteries, Advanced Energy Materials 3 (9) (2013) 1186–1194, https://doi.org/10.1002/aenm.201300139.
[17] M. Zarrabeitia, E. Castillo-Martínez, J.M. López Del Amo, A. Eguía-Barrio, M.Á. Muñoz-Márquez, T. Rojo, M. Casas-Cabanas, Identification of the critical synthesis parameters for enhanced cycling stability of Na-ion anode material $Na_2Ti_3O_7$, Acta Mater. 104 (2016) 125–130, https://doi.org/10.1016/j.actamat.2015.11.033.
[18] X. Wang, Y. Li, Y. Gao, Z. Wang, L. Chen, Additive-free sodium titanate nanotube array as advanced electrode for sodium ion batteries, Nanomater. Energy 13 (2015) 687–692, https://doi.org/10.1016/j.nanoen.2015.03.029.
[19] X.-d. Meng, D.-z. Wang, J.-h. Liu, S.-y. Zhang, Preparation and characterization of sodium titanate nanowires from brookite nanocrystallites, Mater. Res. Bull. 39 (14–15) (2004) 2163–2170, https://doi.org/10.1016/j.materresbull.2004.08.011.
[20] T. Gao, H. Fjellvag, P. Norby, Crystal structures of titanate nanotubes: a Raman scattering study, Inorg. Chem. 48 (4) (2009) 1423–1432, https://doi.org/10.1021/ic801508k.
[21] R.R. Djenadic, L.M. Nikolic, K.P. Giannakopoulos, B. Stojanovic, V.V. Srdic, One-dimensional titanate nanostructures: synthesis and characterization, J. Eur. Ceram. Soc. 27 (13–15) (2007) 4339–4343, https://doi.org/10.1016/j.jeurceramsoc.2007.02.156.
[22] C. Wu, Z.-G. Wu, X. Zhang, R. Rajagopalan, B. Zhong, W. Xiang, M. Chen, H. Li, T. Chen, E. Wang, Z. Yang, X. Guo, Insight into the origin of capacity fluctuation of $Na_2Ti_6O_{13}$ anode in sodium ion batteries, ACS Appl. Mater. Interfaces 9 (50) (2017) 43596–43602, https://doi.org/10.1021/acsami.7b11507.
[23] T. Song, S. Ye, H. Liu, Y.-G. Wang, Self-doping of Ti^{3+}into $Na_2Ti_3O_7$ increases both ion and electron conductivity as a high-performance anode material for sodium-ion batteries, J. Alloys Compd. 767 (2018) 820–828, https://doi.org/10.1016/j.jallcom.2018.07.186.
[24] Y.V. Kolen'ko, K.A. Kovnir, A.I. Gavrilov, A.V. Garshev, J. Frantti, O.I. Lebedev, B. R. Churagulov, G. Van Tendeloo, M. Yoshimura, Hydrothermal synthesis and characterization of nanorods of various titanates and titanium dioxide, J. Phys. Chem. B 110 (9) (2006) 4030–4038, https://doi.org/10.1021/jp055687u.
[25] S.-J. Kim, Y.-U. Yun, H.-J. Oh, S.H. Hong, C.A. Roberts, K. Routray, I.E. Wachs, Characterization of hydrothermally prepared titanate nanotube powders by ambient and in situ Raman spectroscopy, J. Phys. Chem. Lett. 1 (1) (2009) 130–135, https://doi.org/10.1021/jz900025r.
[26] Y. Zhang, H. Hou, X. Yang, J. Chen, M. Jing, Z. Wu, X. Jia, X. Ji, Sodium titanate cuboid as advanced anode material for sodium ion batteries, J. Power Sources 305 (2016) 200–208, https://doi.org/10.1016/j.jpowsour.2015.11.101.
[27] Y. Guo, N.-H. Lee, H.-J. Oh, C.-R. Yoon, K.-S. Park, H.-G. Lee, K.-S. Lee, S.-J. Kim, Structure-tunable synthesis of titanate nanotube thin films via a simple hydrothermal process, Nanotechnology 18 (29) (2007), 295608, https://doi.org/10.1088/0957-4484/18/29/295608.
[28] L. Que, F. Yu, L. Zheng, Z.-B. Wang, D. Gu, Tuning lattice spacing in titanate nanowire arrays for enhanced sodium storage and long-term stability, Nanomater. Energy 45 (2018) 337–345, https://doi.org/10.1016/j.nanoen.2018.01.014.
[29] R.A. Zárate, S. Fuentes, A.L. Cabrera, V.M. Fuenzalida, Structural characterization of single crystals of sodium titanate nanowires prepared by hydrothermal process, J. Cryst. Growth 310 (15) (2008) 3630–3637, https://doi.org/10.1016/j.jcrysgro.2008.05.020.
[30] B. Zhang, R. Dugas, G. Rousse, P. Rozier, A.M. Abakumov, J.M. Tarascon, Insertion compounds and composites made by ball milling for advanced sodium-ion batteries, Nat. Commun. 7 (2016) 10308, https://doi.org/10.1038/ncomms10308.
[31] H. Zhu, K. Yang, H. Lan, S. Qian, H. Yu, L. Yan, N. Long, M. Shui, J. Shu, Electrochemical kinetics of $Na_2Ti_3O_7$ as anode material for lithium-ion batteries, J. Electroanal. Chem. 788 (2017) 203–209, https://doi.org/10.1016/j.jelechem.2017.02.013.
[32] M. Dynarowska, J. Kotwiński, M. Leszczynska, M. Marzantowicz, F. Krok, Ionic conductivity and structural properties of $Na_2Ti_3O_7$ anode material, Solid State Ionics 301 (2017) 35–42, https://doi.org/10.1016/j.ssi.2017.01.002.
[33] G. Garcia-Martinez, L.G. Martinez-Gonzalez, J.I. Escalante-García, A.F. Fuentes, Phase evolution induced by mechanical milling in Ln_2O_3:TiO_2 mixtures (Ln=Gd and Dy), Powder Technol. 152 (1–3) (2005) 72–78, https://doi.org/10.1016/j.powtec.2005.02.004.
[34] T. Rojac, Ž. Trtnik, M. Kosec, Mechanochemical reactions in Na_2CO_3–M_2O_5 (M=V, Nb, Ta) powder mixtures: influence of transition-metal oxide on reaction rate, Solid State Ionics 190 (1) (2011) 1–7, https://doi.org/10.1016/j.ssi.2011.03.011.
[35] T. Rojac, M. Kosec, M. Połomska, B. Hilczer, P. Šegedin, A. Bencan, Mechanochemical reaction in the K_2CO_3–Nb_2O_5 system, J. Eur. Ceram. Soc. 29 (14) (2009) 2999–3006, https://doi.org/10.1016/j.jeurceramsoc.2009.04.017.
[36] T. Rojac, O. Masson, R. Guinebretière, M. Kosec, B. Malič, J. Holc, A study of the mechanochemical synthesis of $NaNbO_3$, J. Eur. Ceram. Soc. 27 (5) (2007) 2265–2271, https://doi.org/10.1016/j.jeurceramsoc.2006.07.017.
[37] T. Rojac, M. Kosec, B. Malič, J. Holc, The application of a milling map in the mechanochemical synthesis of ceramic oxides, J. Eur. Ceram. Soc. 26 (16) (2006) 3711–3716, https://doi.org/10.1016/j.jeurceramsoc.2005.11.013.
[38] T. Rojac, M. Kosec, P. Segedin, B. Malic, J. Holc, The formation of a carbonato complex during the mechanochemical treatment of a Na_2CO_3–Nb_2O_5 mixture, Solid State Ionics 177 (33–34) (2006) 2987–2995, https://doi.org/10.1016/j.ssi.2006.08.001.
[39] W. Liu, J. Zhang, Q. Wang, X. Xie, Y. Lou, X. Han, B. Xia, Microsized TiO_2 activated by high-energy ball milling as starting material for the preparation of $Li_4Ti_5O_{12}$ anode material, Powder Technol. 247 (2013) 204–210, https://doi.org/10.1016/j.powtec.2013.07.016.
[40] T. Rojac, A. Benčan, M. Kosec, Mechanism and role of mechanochemical activation in the synthesis of (K,Na,Li)(Nb,Ta)O_3 ceramics, J. Am. Ceram. Soc. 93 (6) (2010) 1619–1625, https://doi.org/10.1111/j.1551-2916.2010.03643.x.
[41] I.R. Beattie, T.R. Gilson, J.S. Anderson, Single crystal laser Raman spectroscopy, Proc. Roy. Soc. Lond. Math. Phys. Sci. 307 (1491) (1997) 407–429, https://doi.org/10.1098/rspa.1968.0199.
[42] F. Tian, Y. Zhang, J. Zhang, C. Pan, Raman spectroscopy: a new approach to measure the percentage of anatase TiO_2 exposed (001) facets, J. Phys. Chem. C 116 (13) (2012) 7515–7519, https://doi.org/10.1021/jp301256h.
[43] T. Ohsaka, F. Izumi, Y. Fujiki, Raman spectrum of anatase, TiO_2, J. Raman Spectrosc. 7 (6) (1978) 321–324, https://doi.org/10.1002/jrs.1250070606.
[44] M.H. Brooker, J.B. Bates, Raman and infrared spectral studies of anhydrous Li_2CO_3 and Na_2CO_3, J. Chem. Phys. 54 (11) (1971) 4788–4796, https://doi.org/10.1063/1.1674754.
[45] T. Arlt, M. Bermejo, M.A. Blanco, L. Gerward, J.Z. Jiang, J. Staun Olsen, J. M. Recio, High-pressure polymorphs of anatase TiO_2, Phys. Rev. B 61 (21) (2000) 14414–14419, https://doi.org/10.1103/PhysRevB.61.14414.
[46] V.V. Boldyrev, K. Tkáčová, Mechanochemistry of solids: past, present, and prospects, J. Mater. Synth. Process. 8 (3) (2000) 121–132, https://doi.org/10.1023/A:1011347706721.
[47] X. Pan, X. Ma, Phase transformations in nanocrystalline TiO_2 milled in different milling atmospheres, J. Solid State Chem. 177 (11) (2004) 4098–4103, https://doi.org/10.1016/j.jssc.2004.08.017.
[48] S. Yin, H. Yamaki, M. Komatsu, Q. Zhang, J. Wang, Q. Tang, F. Saito, T. Sato, Synthesis of visible-light reactive $TiO_{2-x}N_y$ photocatalyst by mechanochemical doping, Solid State Sci. 7 (12) (2005) 1479–1485, https://doi.org/10.1016/j.solidstatesciences.2005.07.004.
[49] P. Balaz, M. Achimovicova, M. Balaz, P. Billik, Z. Cherkezova-Zheleva, J.M. Criado, F. Delogu, E. Dutkova, E. Gaffet, F.J. Gotor, R. Kumar, I. Mitov, T. Rojac, M. Senna, A. Streletskii, K. Wieczorek-Ciurowa, Hallmarks of mechanochemistry: from nanoparticles to technology, Chem. Soc. Rev. 42 (18) (2013) 7571–7637, https://doi.org/10.1039/c3cs35468g.
[50] N. Burgio, A. Iasonna, M. Magini, S. Martelli, F. Padella, Mechanical alloying of the Fe−Zr system. Correlation between input energy and end products, Il Nuovo Cimento D 13 (4) (1991) 459–476, https://doi.org/10.1007/bf02452130.
[51] F.J. Gotor, M. Achimovicova, C. Real, P. Balaz, Influence of the milling parameters on the mechanical work intensity in planetary mills, Powder Technol. 233 (2013) 1–7, https://doi.org/10.1016/j.powtec.2012.08.031.
[52] P. Xiaoyan, C. Yi, M. Xueming, Z. Lihui, Phase transformation of nanocrystalline anatase powders induced by mechanical activation, J. Am. Ceram. Soc. 87 (6) (2004) 1164–1166, https://doi.org/10.1111/j.1551-2916.2004.01164.x.
[53] P. Scherrer, Bestimmung der Größe und der inneren Struktur von Kolloidteilchen mittels Röntgenstrahlen, in: R. Zsigmondy (Ed.), Kolloidchemie Ein Lehrbuch, Springer Berlin, Heidelberg, 1912, pp. 387–409, https://doi.org/10.1007/978-3-662-33915-27.
[54] U. Holzwarth, N. Gibson, The Scherrer equation versus the 'Debye-Scherrer equation, Nat. Nanotechnol. 6 (9) (2011) 534, https://doi.org/10.1038/nnano.2011.145.
[55] Y. Zhao, J. Zhang, Microstrain and grain-size analysis from diffraction peak width and graphical derivation of high-pressure thermomechanics, J. Appl. Crystallogr. 41 (6) (2008) 1095–1108, https://doi.org/10.1107/s0021889808031762.
[56] Č. Jovalekić, M. Zdujić, A. Radaković, M. Mitrić, Mechanochemical synthesis of $NiFe_2O_4$ ferrite, Mater. Lett. 24 (6) (1995) 365–368, https://doi.org/10.1016/0167-577x(95)00120-4.
[57] V. Šepelák, D. Baabe, D. Mienert, D. Schultze, F. Krumeich, F.J. Litterst, K. D. Becker, Evolution of structure and magnetic properties with annealing temperature in nanoscale high-energy-milled nickel ferrite, J. Magn. Magn Mater. 257 (2) (2003) 377–386, https://doi.org/10.1016/S0304-8853(02)01279-9.
[58] T. Verdier, V. Nachbaur, M. Jean, Mechanosynthesis of zinc ferrite in hardened steel vials: influence of ZnO on the appearance of Fe(II), J. Solid State Chem. 178 (11) (2005) 3243–3250, https://doi.org/10.1016/j.jssc.2005.07.033.
[59] I. Odeh, A.-F.D. Lehlooh, S.H. Mahmood, X-ray diffraction and Mössbauer spectroscopy of high energy ball-milled α-Fe_2O_3/TiO_2 composite powders, Hyperfine Interact. 183 (1–3) (2008) 25–29, https://doi.org/10.1007/s10751-008-9802-x.
[60] V.P. Pavlović, J. Krstić, M.J. Šćepanović, J. Dojčilović, D.M. Minić, J. Blanuša, S. Stevanović, V. Mitić, V.B. Pavlović, Structural investigation of mechanically activated nanocrystalline $BaTiO_3$ powders, Ceram. Int. 37 (7) (2011) 2513–2518, https://doi.org/10.1016/j.ceramint.2011.03.064.
[61] O. Helgason, J.Z. Jiang, High-temperature mössbauer spectroscopy of mechanically milled $NiFe_2O_4$, Hyperfine Interact. 139 (1) (2002) 325–333, https://doi.org/10.1023/A:1021285720151.
[62] J. Wang, J.M. Xue, D.M. Wan, B.K. Gan, Mechanically activating nucleation and growth of complex perovskites, J. Solid State Chem. 154 (2) (2000) 321–328, https://doi.org/10.1006/jssc.2000.8782.
[63] R.L. Penn, J.F. Banfield, Imperfect oriented attachment: dislocation generation in defect-free nanocrystals, Science 281 (5379) (1998) 969–971, https://doi.org/10.1126/science.281.5379.969.

[64] R.L. Penn, J.F. Banfield, Morphology development and crystal growth in nanocrystalline aggregates under hydrothermal conditions: insights from titania, Geochem. Cosmochim. Acta 63 (10) (1999) 1549–1557, https://doi.org/10.1016/s0016-7037(99)00037-x.
[65] R. Merkle, J. Maier, On the tammann–rule, Z. Anorg. Allg. Chem. 631 (6-7) (2005) 1163–1166, https://doi.org/10.1002/zaac.200400540.
[66] C.E. Bamberger, G.M. Begun, Sodium titanates: stoichiometry and Raman spectra, J. Am. Ceram. Soc. 70 (3) (1987) C48–C51, https://doi.org/10.1111/j.1151-2916.1987.tb04963.x.
[67] Y. Su, M.L. Balmer, B.C. Bunker, Raman spectroscopic studies of silicotitanates, J. Phys. Chem. B 104 (34) (2000) 8160–8169, https://doi.org/10.1021/jp0018807.
[68] S. Papp, L. Kőrösi, V. Meynen, P. Cool, E.F. Vansant, I. Dékány, The influence of temperature on the structural behaviour of sodium tri- and hexa-titanates and their protonated forms, J. Solid State Chem. 178 (5) (2005) 1614–1619, https://doi.org/10.1016/j.jssc.2005.03.001.
[69] Y. Xu, D. Bauer, M. Lübke, T.E. Ashton, Y. Zong, J.A. Darr, High-power sodium titanate anodes; a comparison of lithium vs sodium-ion batteries, J. Power Sources 408 (2018) 28–37, https://doi.org/10.1016/j.jpowsour.2018.10.038.
[70] H. Liu, D. Yang, Z. Zheng, X. Ke, E. Waclawik, H. Zhu, R.L. Frost, A Raman spectroscopic and TEM study on the structural evolution of $Na_2Ti_3O_7$ during the transition to $Na_2Ti_6O_{13}$, J. Raman Spectrosc. 41 (10) (2010) 1331–1337, https://doi.org/10.1002/jrs.2561.
[71] H. Liu, D. Yang, E.R. Waclawik, X. Ke, Z. Zheng, H. Zhu, R.L. Frost, A Raman spectroscopic study on the active site of sodium cations in the structure of $Na_2Ti_3O_7$ during the adsorption of Sr^{2+} and Ba^{2+} cations, J. Raman Spectrosc. 41 (12) (2010) 1792–1796, https://doi.org/10.1002/jrs.2634.
[72] M. Shirpour, J. Cabana, M. Doeff, New materials based on a layered sodium titanate for dual electrochemical Na and Li intercalation systems, Energy Environ. Sci. 6 (8) (2013) 2538–2547, https://doi.org/10.1039/c3ee41037d.
[73] F.L.R.e. Silva, A.A.A. Filho, M.B. da Silva, K. Balzuweit, J.-L. Bantignies, E.W. S. Caetano, R.L. Moreira, V.N. Freire, A. Righi, Polarized Raman, FTIR, and DFT study of $Na_2Ti_3O_7$ microcrystals, J. Raman Spectrosc. 49 (3) (2018) 538–548, https://doi.org/10.1002/jrs.5316.
[74] K. Teshima, S. Lee, S. Murakoshi, S. Suzuki, K. Yubuta, T. Shishido, M. Endo, S. Oishi, Highly crystalline, idiomorphic $Na_2Ti_6O_{13}$ whiskers grown from a NaCl flux at a relatively low temperature, Eur. J. Inorg. Chem. 19 (2010) 2936–2940, https://doi.org/10.1002/ejic.200901175, 2010.
[75] J. Wang, J. Bi, W. Wang, Z. Xing, Y. Bai, M. Leng, X. Gao, $Na_2Ti_6O_{13}$ coated with carbon produced by citric acid as an anode material in sodium ion batteries, J. Electrochem. Soc. 167 (9) (2020), 090539, https://doi.org/10.1149/1945-7111/ab8fd6.
[76] K. Cao, L. Jiao, W.K. Pang, H. Liu, T. Zhou, Z. Guo, Y. Wang, H. Yuan, $Na_2Ti_6O_{13}$ nanorods with dominant large interlayer spacing exposed facet for high-performance Na-ion batteries, Small 12 (22) (2016) 2991–2997, https://doi.org/10.1002/smll.201600845.
[77] L. Luo, Y. Zhen, Y. Lu, K. Zhou, J. Huang, Z. Huang, S. Mathur, Z. Hong, Structural evolution from layered $Na_2Ti_3O_7$ to $Na_2Ti_6O_{13}$ nanowires enabling a highly reversible anode for Mg-ion batteries, Nanoscale 12 (1) (2020) 230–238, https://doi.org/10.1039/c9nr08003a.
[78] M. Zarrabeitia, E. Castillo-Martínez, J.M. López Del Amo, A. Eguía-Barrio, M. A. Muñoz-Márquez, T. Rojo, M. Casas-Cabanas, Towards environmentally friendly Na-ion batteries: moisture and water stability of $Na_2Ti_3O_7$, J. Power Sources 324 (2016) 378–387, https://doi.org/10.1016/j.jpowsour.2016.05.103.
[79] H. Höchst, R.D. Bringans, P. Steiner, T. Wolf, Photoemission study of the electronic structure of stoichiometric and substoichiometric TiN and ZrN, Phys. Rev. B 25 (12) (1982) 7183–7191, https://doi.org/10.1103/physrevb.25.7183.
[80] I. Bertóti, M. Mohai, J.L. Sullivan, S.O. Saied, Surface characterisation of plasma-nitrided titanium: an XPS study, Appl. Surf. Sci. 84 (4) (1995) 357–371, https://doi.org/10.1016/0169-4332(94)00545-1.
[81] L.P. Wang, L. Yu, X. Wang, M. Srinivasan, Z.J. Xu, Recent developments in electrode materials for sodium-ion batteries, J. Mater. Chem. 3 (18) (2015) 9353–9378, https://doi.org/10.1039/c4ta06467d.
[82] S. Nandan, T.G. Deepak, S.V. Nair, A.S. Nair, TiO_2 nanofibers resembling 'yellow bristle grass' in morphology by a soft chemical transformation, Dalton Trans. 44 (20) (2015) 9637–9645, https://doi.org/10.1039/c5dt01027f.
[83] J. Ni, S. Fu, C. Wu, Y. Zhao, J. Maier, Y. Yu, L. Li, Superior sodium storage in $Na_2Ti_3O_7$ nanotube Arrays through surface engineering, Adv. Energy Mater. 6 (11) (2016), 1502568, https://doi.org/10.1002/aenm.201502568.
[84] D. Kong, Y. Wang, S. Huang, Y.V. Lim, J. Zhang, L. Sun, B. Liu, T. Chen, P. Valdivia y Alvarado, H.Y. Yang, Surface modification of $Na_2Ti_3O_7$ nanofibre arrays using N-doped graphene quantum dots as advanced anodes for sodium-ion batteries with ultra-stable and high-rate capability, J. Mater. Chem. 7 (20) (2019) 12751–12762, https://doi.org/10.1039/c9ta01641d.
[85] S.P. Kowalczyk, L. Ley, F.R. McFeely, R.A. Pollak, D.A. Shirley, X-ray photoemission from sodium and lithium, Phys. Rev. B 8 (8) (1973) 3583–3585, https://doi.org/10.1103/physrevb.8.3583.
[86] R.A. Zárate, S. Fuentes, J.P. Wiff, V.M. Fuenzalida, A.L. Cabrera, Chemical composition and phase identification of sodium titanate nanostructures grown from titania by hydrothermal processing, J. Phys. Chem. Solid. 68 (4) (2007) 628–637, https://doi.org/10.1016/j.jpcs.2007.02.011.
[87] M.A. Muñoz-Márquez, M. Zarrabeitia, E. Castillo-Martínez, A. Eguía-Barrio, T. Rojo, M. Casas-Cabanas, Composition and evolution of the solid-electrolyte interphase in $Na_2Ti_3O_7$ electrodes for Na-ion batteries: XPS and auger parameter analysis, ACS Appl. Mater. Interfaces 7 (14) (2015) 7801–7808, https://doi.org/10.1021/acsami.5b01375.
[88] G. Greczynski, L. Hultman, X-ray photoelectron spectroscopy: towards reliable binding energy referencing, Prog. Mater. Sci. 107 (2020) 100591–100636, https://doi.org/10.1016/j.pmatsci.2019.100591.
[89] I. Song, H. Lee, D.H. Kim, Rotation-Assisted hydrothermal synthesis of thermally stable multiwalled titanate nanotubes and their application to selective catalytic reduction of NO with NH_3, ACS Appl. Mater. Interfaces 10 (49) (2018) 42249–42257, https://doi.org/10.1021/acsami.8b14589.
[90] N.D. Trinh, O. Crosnier, S.B. Schougaard, T. Brousse, Synthesis, Characterization and electrochemical studies of active materials for sodium ion batteries, ECS Trans 35 (32) (2011) 91–98, https://doi.org/10.1149/1.3655691.
[91] L. Takacs, J.S. McHenry, Temperature of the milling balls in shaker and planetary mills, J. Mater. Sci. 41 (16) (2006) 5246–5249, https://doi.org/10.1007/s10853-006-0312-4.
[92] J. Tang, A.P. Alivisatos, Crystal splitting in the growth of Bi_2S_3, Nano Lett. 6 (12) (2006) 2701–2706, https://doi.org/10.1021/nl0615930.
[93] B. Malic, D. Jenko, J. Holc, M. Hrovat, M. Kosec, Synthesis of sodium potassium niobate: a diffusion couples study, J. Am. Ceram. Soc. 91 (6) (2008) 1916–1922, https://doi.org/10.1111/j.1551-2916.2008.02376.x.
[94] M.-J. Li, Z.-Y. Chi, Y.-C. Wu, Morphology, chemical composition and phase transformation of hydrothermal derived sodium titanate, J. Am. Ceram. Soc. 95 (10) (2012) 3297–3304, https://doi.org/10.1111/j.1551-2916.2012.05330.x.
[95] M.M. Doeff, J. Cabana, M. Shirpour, Titanate anodes for sodium ion batteries, J. Inorg. Organomet. Polym. Mater. 24 (1) (2014) 5–14, https://doi.org/10.1007/s10904-013-9977-8.
[96] M.A. Morris, D.G. Morris, Ball-milling of elemental powders-compound formation and/or amorphization, J. Mater. Sci. 26 (17) (1991) 4687–4696, https://doi.org/10.1007/bf00612407.